



Local and Global Dynamics in Intrinsically Disordered Synuclein

Nasrollah Rezaei-Ghaleh, Giacomo Parigi, Andrea Soranno, Andrea Holla, Stefan Becker, Benjamin Schuler, Claudio Luchinat,* and Markus Zweckstetter*

Abstract: Intrinsically disordered proteins (IDPs) experience a diverse spectrum of motions that are difficult to characterize with a single experimental technique. Herein we combine high- and low-field nuclear spin relaxation, nanosecond fluorescence correlation spectroscopy (nsFCS), and long molecular dynamics simulations of alpha-synuclein, an IDP involved in Parkinson disease, to obtain a comprehensive picture of its conformational dynamics. The combined analysis shows that fast motions below 2 ns caused by local dihedral angle fluctuations and conformational sampling within and between Ramachandran substates decorrelate most of the backbone *N*–*H* orientational memory. However, slow motions with correlation times of up to ca. 13 ns from segmental dynamics are present throughout the alpha-synuclein chain, in particular in its C-terminal domain, and global chain reconfiguration occurs on a timescale of ca. 60 ns. Our study demonstrates a powerful strategy to determine residue-specific protein dynamics in IDPs at different time and length scales.

Intrinsically disordered proteins (IDPs) constitute a large fraction of the eukaryotic proteome and play key roles in many cellular processes.^[1] The biological function of IDPs is supported by their high mobility,^[2] which arises because of the flat energy landscape of IDPs compared to folded proteins. As a result, IDPs are best described as heterogeneous ensembles of rapidly interconverting structures^[3] and several ensembles have been proposed based on conformationally averaged structural restraints.^[4] Frequently, disease-related

mutations and posttranslational modifications do not seem to significantly alter the structural properties of IDPs, suggesting that their pathological effect may be caused by changes in protein dynamics. Nevertheless, a comprehensive picture of the dynamics of IDPs is still lacking. One of the major challenges is that dynamics in IDPs occur over a broad range of length- and timescales that are difficult to cover with a single experimental technique. Herein we combine three experimental techniques—high-field ¹⁵N spin relaxation, low-field ¹H relaxometry, and nanosecond fluorescence correlation spectroscopy (nsFCS)—which are sensitive to motions on different length and timescales, with long molecular dynamics (MD) simulations to obtain insight into local and global dynamics from one to hundreds of nanoseconds in the IDP alpha-synuclein (aS; Supporting Information, Figure S1).

The starting point of our study was the 16-μs MD trajectory for aS, which was previously calculated at 300 K using the Amber12 force field and the TIP4P-D water model with 2.5 fs time steps and saved at 10 ps time intervals.^[5] Because of its long simulation time, this MD trajectory extensively samples aS's conformational space and dynamics (Figure 1 a). ¹H relaxometry (0.1–50 MHz) of aS was previously recorded^[6] (Figure 1 b), while nsFCS and single-molecule Förster resonance energy transfer (smFRET) experiments (Figure 1 c), as well as high-field ¹⁵N spin relaxation rates (Figure 1 f–h) were measured in the current study.

First, we asked whether the motions sampled in the MD trajectory are in agreement with experimental ¹H relaxometry data. To this end, we calculated from the MD trajectory angular autocorrelation functions (ACFs) and spectral density functions for all H_α, methylene, and methyl protons. From the spectral density functions, individual ¹H *R*₁ rates were predicted at different fields (Supporting Information, Methods). The calculated ACFs required a 4-exponential decay function to be fitted (Figure S2 a), with the longest correlation times showing a large variation (Figure S2). The average second correlation time was 1.6 ns. The global *R*₁ dispersion profile was then simulated and compared with experiment (Figure 1 b). When the simulated profile was fitted to a single correlation time equation (Supporting Information, Eq. S6 a),^[7] it resulted in $S_C^2 = 0.10 \pm 0.01$, $\tau_R = 5.8 \pm 0.3$ ns and $\alpha = 5.0 \pm 0.5$ s⁻¹. These values are in good agreement with the parameters obtained from a fit of the experimental profile ($S_C^2 = 0.08 \pm 0.01$, $\tau_R = 6.3 \pm 0.4$ ns and $\alpha = 6.1 \pm 0.3$ s⁻¹ in water solution).^[6] The quality of the fit to the MD-predicted relaxometry profile improved when two correlation times were included (Eq. S6 b). This is expected because a distribution of correlation times is at the origin of the simulated data (Figure S2 b). Subsequently, the shorter correlation time (τ_{R2}) was fixed to 1.6 ns (see above), because of its large covariance with the corresponding order param-

[*] Dr. N. Rezaei-Ghaleh, Prof. M. Zweckstetter
University Medical Center Göttingen & German Center for Neurodegenerative Diseases (DZNE) & MPI for Biophysical Chemistry
Von-Siebold-Strasse 3a, 37075 Göttingen (Germany)
E-mail: markus.zweckstetter@dzne.de

Prof. G. Parigi, Prof. C. Luchinat
Magnetic Resonance Center (CERM) & Department of Chemistry
"Ugo Schiff"
University of Florence
via Sacconi 6, 50121 Sesto Fiorentino (Italy)
E-mail: luchinat@cerm.unifi.it

Prof. A. Soranno
Washington University in St. Louis
St. Louis, MO 63110 (USA)

Prof. A. Soranno, Dr. A. Holla, Prof. B. Schuler
University of Zurich
8057 Zurich (Switzerland)

Dr. S. Becker
Max Planck Institute for Biophysical Chemistry
Am Fassberg 11, 37077 Göttingen (Germany)

Supporting information and the ORCID identification number(s) for the author(s) of this article can be found under:
<https://doi.org/10.1002/anie.201808172>.

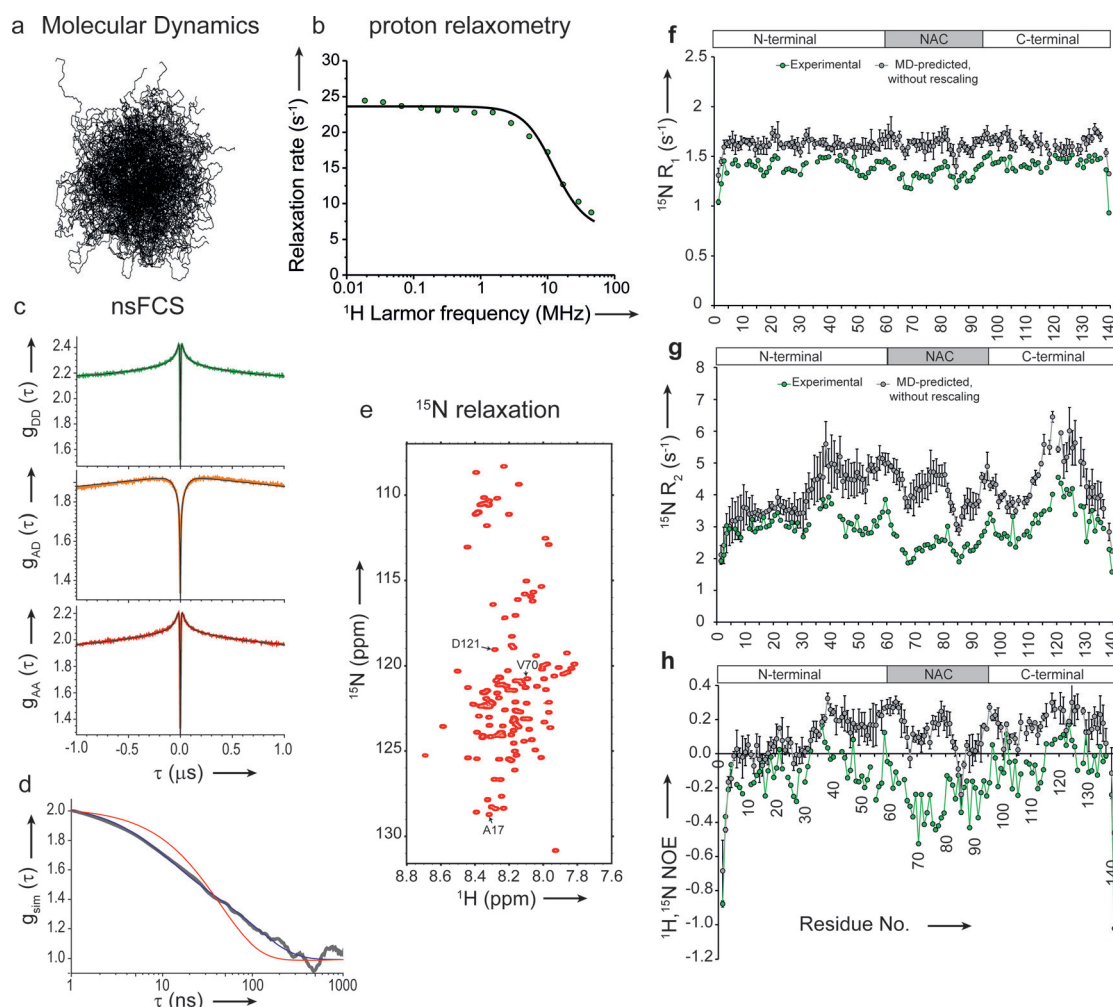


Figure 1. Integrative analysis of the local and global dynamics of aS. a) Representative ensemble of aS from a 16- μ s-long MD simulation. b) ^1H relaxometry measured in D_2O (circles) superimposed on the MD simulated profile (solid line; rescaled to account for different viscosities of H_2O and D_2O). c), d) Experimental nsFCS (c) and the auto-correlation of the S42-T92 C^α - C^α distance calculated from the MD trajectory (d). Compared to a single-exponential decay (red curve), the fit with a two-exponential decay function (purple curve) improved. Derived correlation times are similar to those obtained from the global fit of the experimental auto- and cross-correlations. e) A typical ^{15}N , ^1H correlation spectrum, with three residues from the N-terminal, NAC and C-terminal regions (A17, V70 and D121) highlighted (see Supporting Information, Figure S4). f)–h) ^{15}N R_1 and R_2 rates and hetNOEs, measured (green circles/lines) and calculated from the MD trajectory (gray; at 600 MHz). Error bars for simulated R_1/R_2 represent the standard deviation between rates calculated from three MD sub-trajectories, each of 5 μs duration. Error bars for experimental rates are smaller than the symbol size.

eter, $S_{\text{C}(2)}^2$. The resulting best fit values for $\tau_{\text{R}1}$, $S_{\text{C}(1)}^2$, and $S_{\text{C}(2)}^2$ were 8.7 ± 0.5 ns, 0.044 ± 0.004 , and 0.25 ± 0.02 , respectively. When the experimental profile was similarly fitted, the best fit values for $\tau_{\text{R}1}$, $S_{\text{C}(1)}^2$ and $S_{\text{C}(2)}^2$ were 8.6 ± 1.6 ns, 0.05 ± 0.02 and 0.16 ± 0.09 , respectively. The analysis shows that a state-of-the-art MD force field/water model is capable of capturing slow motions, which modulate ^1H - ^1H dipolar interactions with a τ_{R} of 6–9 ns.

smFRET and nsFCS have recently emerged as powerful techniques to study disordered proteins.^[8] They rely on the distance-dependent coupling of the electronic transition dipoles of a donor and acceptor fluorophore attached to the polypeptide chain and enable access to longer timescales than ^1H relaxometry, typically in the range of tens to hundreds of nanoseconds for IDPs. To allow labeling of aS with Alexa 488/594 as donor/acceptor, we prepared a double-cysteine variant

of aS (S42C/T92C aS). In smFRET a mean transfer efficiency of 0.64 was obtained, corresponding to a root-mean-squared (rms) inter-residue distance of 4.5 ± 0.4 nm, close to the rms distance of 4.4 ± 0.2 nm calculated from the MD simulation (Figure S3 and Table S1). The observed fluorescence intensity correlation functions showed characteristic correlated and anti-correlated components in the sub-microsecond range in the auto-correlation and donor-acceptor cross-correlation functions, respectively (Figure 1c). From a global analysis of all correlation functions obtained by nsFCS with a single-exponential decay, a reconfiguration time τ_{r} of 58 ± 13 ns was determined. The τ_{r} value of aS is within the typical range obtained for other disordered proteins of similar length^[8b,9] and can be directly compared with the corresponding distance correlation time from the MD simulation of aS. Indeed, we obtained a mean relaxation time of 43 ns (Figure 1d) from

a single-exponential fit of the MD distance correlation, only slightly smaller than the experimental value. However, we also observed that the MD-based correlation function was better described by a double-exponential decay with two correlation times of 10 ± 2 ns (amplitude $41 \pm 5\%$) and 107 ± 16 ns ($59 \pm 5\%$). A similar analysis of the experimental correlations resulted in correlation times of 23 ± 4 ns ($66 \pm 2\%$) and 136 ± 33 ns ($34 \pm 2\%$). The weighted average of the two correlation times was 67 ± 12 ns from MD simulation and 61 ± 14 ns from nsFCS data. The analyses/measurements suggest that the MD trajectory of aS captures with good accuracy the motional timescales probed by ^1H relaxometry and nsFCS.

A particularly powerful technique for the study of protein dynamics is high-field ^{15}N spin relaxation, because it provides access to dynamics from tens of picoseconds to several nanoseconds with single-residue resolution.^[10] We measured different ^{15}N relaxation rates for aS at conditions identical to those used in the ^1H relaxometry experiments (1 mM aS, pH 5.0, 25 °C;^[6]). Consistent with previous reports,^[11] the central NAC region (residues 60–95) exhibited transverse relaxation (R_2) rates smaller than the average, while residues 115–130 in the C-terminus had larger R_2 rates (Figure 1 d–h; Figures S4,S5).^[11a] Importantly, highly similar relaxation rates were obtained at lower aS concentration (150 μM , Figure S6), excluding significant contributions from oligomerization. In addition, similar R_2 rates were derived from cross-correlated relaxation measurements (Figure S7), indicating that exchange processes do not contribute to the observed R_2 rates.

Several theoretical frameworks have been developed for the analysis of ^{15}N relaxation data in IDPs.^[10b,12] We first performed spectral density mapping.^[13] The analysis showed that aS backbone dynamics cannot be described by a single correlation time, consistent with the disordered nature of aS (Figure S8). Next, we calculated angular ACFs for 134 individual backbone N-Hs of aS from the MD trajectory (see Supporting Information Methods, Figure S9 and Table S2). On the basis of a three-exponential fit, average correlation times for the fast, intermediate, and slow motions of 145 ± 42 ps, 1.53 ± 0.43 ns, and 7.02 ± 1.82 ns were obtained. Corresponding order parameters were 0.26 ± 0.05 , 0.49 ± 0.04 , and 0.26 ± 0.07 for S_{fast}^2 , S_{int}^2 , and S_{slow}^2 , respectively (Figure S10).

Individual ACFs were also directly converted to spectral density functions through Fourier transformation, and residue-specific ^{15}N relaxation rates were predicted and compared with experiment (Figure 1 f,g; Figure S5). Predicted ^{15}N R_2 and CCR values, and to a lesser extent R_1 values, were larger than the experimental values, in agreement with an overestimation of $J(0)$ and $J(\omega_{\text{N}})$ by MD (Figure S8). The comparison between experimental and predicted hetNOEs further indicated that the fast sub-nanosecond motions represented by $J(\omega_{\text{H}})$ are underestimated by the MD trajectory (Figure 1 h). The origin of these discrepancies could be limitations in accurately capturing the timescales or amplitudes of motions in the MD trajectory.

With regard to potential temporal limitations, we found that a scaling factor of approximately 0.55 of the time axis of the MD trajectory would be required to match the exper-

imental average ^{15}N relaxation rates (Figure S11 and Table S3). However, this seems excluded by the good agreement between the correlation times obtained from experimental and MD-based ^1H relaxometry profiles and nsFCS data. We therefore used the ^{15}N relaxation data to investigate potential restrictions of the backbone flexibility in MD. On the basis of R_1 and R_2 at 600 MHz, residue-specific scaling factors for S_{fast}^2 , S_{int}^2 , and S_{slow}^2 were determined (Figure 2a, Figure S12a), while the scaling factor for the time axis was

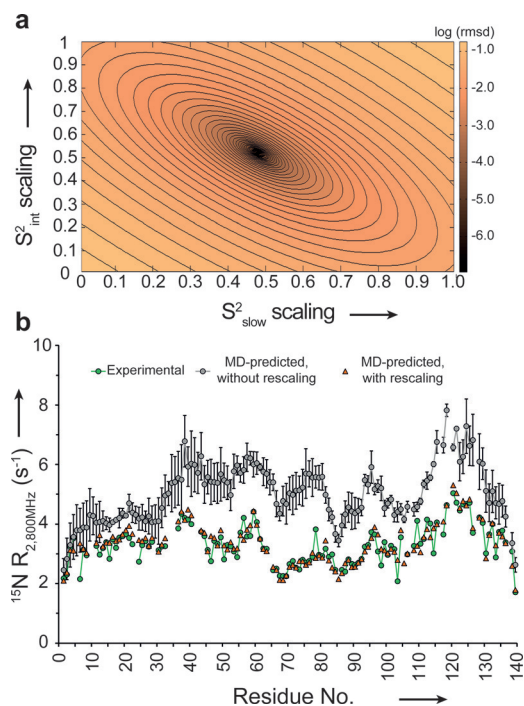


Figure 2. Order parameter optimization on the basis of ^{15}N R_1 and R_2 (at 600 MHz) of aS. a) Fit quality depends on rescaling of intermediate and slow squared order parameters (S_{int}^2 , S_{slow}^2), shown here for Y39. A minimum was found for S_{int}^2 and S_{slow}^2 scaling factors of approximately 0.52 and 0.48, respectively. b) Cross-validation by ^{15}N R_2 at 800 MHz. Simulated rates calculated on the basis of rescaled order parameters (orange) match experimental rates (green).

1.05 ± 0.05 (Figure S12 b), that is, effectively no scaling for the time axis in agreement with the results comparing ^1H relaxometry and nsFCS with MD. Notably, a global rescaling factor for example for S_{slow}^2 was not sufficient (SI, Figure S11 and Table S3). This is expected because there are many modes of motion in protein backbone and side chains that overall affect N–H reorientation in IDPs such that different residues in the sequence might experience different levels of reorientational dynamic limitations by current MD force fields.

Experimental ^{15}N relaxation rates were best predicted from the MD simulation with scaling factors of 0.52 ± 0.08 for S_{fast}^2 , 0.33 ± 0.05 for S_{int}^2 and 0.15 ± 0.06 for S_{slow}^2 . Cross-validation using experimental CCR at 600 MHz and R_2 at 800 MHz demonstrated the reliability of the determined scaling factors (Figure 2 b, Figure S13). In addition, different regions of aS required different levels of scaling, with residues 60–90 demanding the highest degree of S_{slow}^2 scaling (Fig-

ure S14). The required order-parameter scaling suggests that local flexibility is over-restricted in the MD simulation of aS.

Our study provides a detailed, residue-specific view of the backbone dynamics of the paradigmatic IDP aS. For most aS residues, fast motions reporting librational motions and local ϕ/ψ dihedral angle fluctuations decorrelate approximately 52% of N–H orientational memory, intermediate motions with correlation times of about 1.6 ns, reporting broader conformational sampling within and between Ramachandran substates, decorrelate approximately 33% of N–H orientations, and around 15% of correlation is relaxed by slow motions with correlation times of approximately 6–13 ns, representing segmental dynamics of the disordered aS chain (Figure 3). In addition, we found that the NAC region

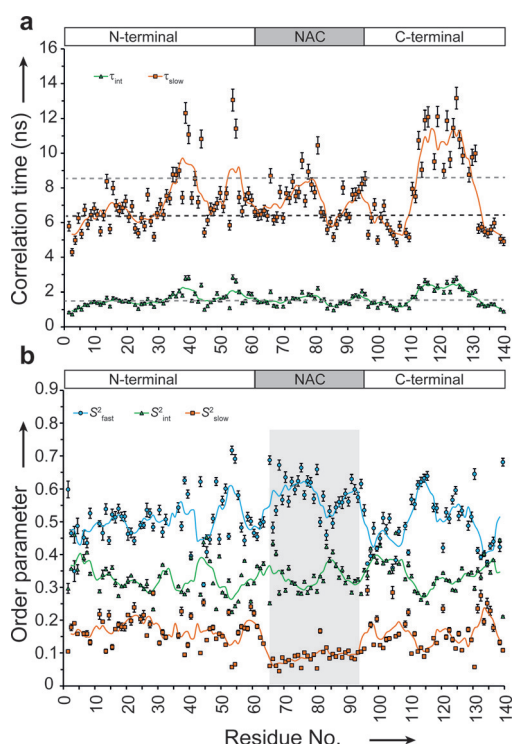


Figure 3. Residue-specific correlation times (a) and squared order parameters (b) of aS, obtained after time-axis rescaling (by a factor of 1.05 ± 0.05) of the MD trajectory and optimization of MD-based order parameters. In (a), dashed lines represent the correlation times obtained after fitting of the experimental ^1H relaxometry profile to equations with single (black line) or two (gray line) correlation times. Solid lines show values averaged over a five-residue window.

possesses smaller amplitudes of slow motions ($S^2_{\text{slow}} = 0.09 \pm 0.02$) than the N- and C-terminal residues. The conversion from an intrinsically disordered structure in solution to an ordered structure in aS fibrils demands extensive conformational rearrangements, in which the high level of backbone dynamics in the NAC region, which forms the core of aS fibrils,^[14] may play a supporting role. Another finding from our study is that five residues (Y39, V40, T44, T54, and V55) in the N-terminal half of aS have very large τ_{slow} values, exceeding 10 ns (Figure 3a). We note that Y39 plays an important role for aggregation of aS into amyloid fibrils.^[15]

Although we currently do not understand the detailed connection between backbone dynamics of aS and its pathological aggregation, the data suggest that local and global dynamics in the monomeric state of aS might be important for its pathogenic aggregation.

Furthermore, the distinct dynamical features of the N-terminal region of aS may support its role in aS binding to lipid membranes.^[16] In contrast to the interactions between folded proteins, IDPs can make long-range interactions, and their chain dynamics will thus directly contribute to the mechanisms of binding.^[17] Further insight into aS functions could be achieved when the spectrum of motions is obtained for aS and its disease-related variants under different conditions.

Previous approaches for the analysis of IDP dynamics differentially weighted sequential snapshots in MD trajectories to reproduce experimental order parameters.^[18] Alternatively, multi-timescale dynamics of IDPs have been investigated through a large set of ^{15}N relaxation rates at different fields to derive timescales and order parameters of motions.^[19] In contrast, the integrative approach presented herein benefits from the unique advantages of low-field ^1H relaxometry and nsFCS to directly access timescale information, especially for slower motions, and is thus expected to be less affected by coupling of motions on different timescales. In summary, our study shows that the combination of experimental techniques with complementary sensitivity to protein dynamics and their integration with MD simulations is a powerful strategy to characterize dynamics in IDPs on a wide range of time and length scales. Ultimately, the accurate description of multiscale dynamics in the disordered state of proteins paves the way for a high-resolution understanding of protein folding and misfolding.

Acknowledgements

This work was supported by the advanced grant ‘787679 - LLPS-NMR’ of the European Research Council (to M.Z.), the Fondazione Cassa di Risparmio di Firenze, MIUR PRIN 2012SK7ASN, European Commission (contracts Propagating 634821 and iNEXT 653706), COST Action CA15209 (EURELAX), the EU ESFRI Instruct Core Centre CERM, the Swiss National Science Foundation (to B.S.), and the Deutsche Forschungsgemeinschaft (RE 3655/2-1, to N.R.-G.). We thank D.E. Shaw Research for sharing their a-synuclein simulation data and Karin Giller for excellent technical help with protein preparation.

Conflict of interest

The authors declare no conflict of interest.

Keywords: intrinsically disordered proteins · NMR spectroscopy · protein dynamics

How to cite: *Angew. Chem. Int. Ed.* **2018**, *57*, 15262–15266
Angew. Chem. **2018**, *130*, 15482–15486

- [1] S. DeForte, V. N. Uversky, *Molecules* **2016**, *21*, 1090.
- [2] I. C. Felli, R. Pierattelli, *Intrinsically Disordered Proteins Studied by NMR Spectroscopy*, 1st ed., Springer, Berlin, **2015**.
- [3] a) N. Rezaei-Ghaleh, M. Blackledge, M. Zweckstetter, *ChemBioChem* **2012**, *13*, 930–950; b) M. R. Jensen, R. W. Ruigrok, M. Blackledge, *Curr. Opin. Struct. Biol.* **2013**, *23*, 426–435.
- [4] a) L. Salmon, G. Nodet, V. Ozenne, G. Yin, M. R. Jensen, M. Zweckstetter, M. Blackledge, *J. Am. Chem. Soc.* **2010**, *132*, 8407–8418; b) J. R. Allison, P. Varnai, C. M. Dobson, M. Vendruscolo, *J. Am. Chem. Soc.* **2009**, *131*, 18314–18326; c) O. Ullman, C. K. Fisher, C. M. Stultz, *J. Am. Chem. Soc.* **2011**, *133*, 19536–19546; d) T. Hošek, E. O. Calcada, M. O. Nogueira, M. Salvi, T. D. Pagani, I. C. Felli, R. Pierattelli, *Chemistry* **2016**, *22*, 13010–13013.
- [5] S. Piana, A. G. Donchev, P. Robustelli, D. E. Shaw, *J. Phys. Chem. B* **2015**, *119*, 5113–5123.
- [6] G. Parigi, N. Rezaei-Ghaleh, A. Giachetti, S. Becker, C. Fernandez, M. Blackledge, C. Griesinger, M. Zweckstetter, C. Luchinat, *J. Am. Chem. Soc.* **2014**, *136*, 16201–16209.
- [7] C. Luchinat, G. Parigi, *J. Am. Chem. Soc.* **2007**, *129*, 1055–1064.
- [8] a) H. S. Chung, K. McHale, J. M. Louis, W. A. Eaton, *Science* **2012**, *335*, 981–984; b) D. Nettels, I. V. Gopich, A. Hoffmann, B. Schuler, *Proc. Natl. Acad. Sci. USA* **2007**, *104*, 2655–2660.
- [9] a) A. Soranno, B. Buchli, D. Nettels, R. R. Cheng, S. Muller-Spath, S. H. Pfeil, A. Hoffmann, E. A. Lipman, D. E. Makarov, B. Schuler, *Proc. Natl. Acad. Sci. USA* **2012**, *109*, 17800–17806; b) M. Aznauryan, L. Delgado, A. Soranno, D. Nettels, J. R. Huang, A. M. Labhardt, S. Grzesiek, B. Schuler, *Proc. Natl. Acad. Sci. USA* **2016**, *113*, E5389–E5398; c) B. Schuler, H. Hofmann, A. Soranno, D. Nettels, *Annu. Rev. Biophys.* **2016**, *45*, 207–231; d) A. Soranno, A. Holla, F. Dingfelder, D. Nettels, D. E. Makarov, B. Schuler, *Proc. Natl. Acad. Sci. USA* **2017**, *114*, E1833–E1839.
- [10] a) N. Salvi, A. Abyzov, M. Blackledge, *Prog. Nucl. Magn. Reson. Spectrosc.* **2017**, *102–103*, 43–60; b) M. L. Gill, R. A. Byrd, A. G. Palmer III, *Phys. Chem. Chem. Phys.* **2016**, *18*, 5839–5849.
- [11] a) R. Bussell, Jr., D. Eliezer, *J. Biol. Chem.* **2001**, *276*, 45996–46003; b) S. McClendon, C. C. Rospigliosi, D. Eliezer, *Protein Sci.* **2009**, *18*, 1531–1540; c) T. S. Ulmer, A. Bax, *J. Biol. Chem.* **2005**, *280*, 43179–43187.
- [12] a) N. A. Farrow, O. Zhang, J. D. Forman-Kay, L. E. Kay, *Biochemistry* **1997**, *36*, 2390–2402; b) P. Kadeřávek, V. Zapletal, A. Rabatinová, L. Krásný, V. Sklenář, L. Židek, *J. Biomol. NMR* **2014**, *58*, 193–207; c) M. Buck, H. Schwalbe, C. M. Dobson, *J. Mol. Biol.* **1996**, *257*, 669–683; d) K. Modig, F. M. Poulsen, *J. Biomol. NMR* **2008**, *42*, 163–177; e) S. N. Khan, C. Charlier, R. Augustyniak, N. Salvi, V. Dejean, G. Bodenhausen, O. Lequin, P. Pelupessy, F. Ferrage, *Biophys. J.* **2015**, *109*, 988–999; f) J. J. Prompers, R. Bruschweiler, *J. Am. Chem. Soc.* **2002**, *124*, 4522–4534.
- [13] N. A. Farrow, O. Zhang, J. D. Forman-Kay, L. E. Kay, *Biochemistry* **1995**, *34*, 868–878.
- [14] M. D. Tuttle, G. Comellas, A. J. Nieuwkoop, D. J. Covell, D. A. Berthold, K. D. Kloepper, J. M. Courtney, J. K. Kim, A. M. Barclay, A. Kendall, W. Wan, G. Stubbs, C. D. Schwieters, V. M. Lee, J. M. George, C. M. Rienstra, *Nat. Struct. Mol. Biol.* **2016**, *23*, 409–415.
- [15] R. M. Rasia, C. W. Bertoncini, D. Marsh, W. Hoyer, D. Cherny, M. Zweckstetter, C. Griesinger, T. M. Jovin, C. O. Fernandez, *Proc. Natl. Acad. Sci. USA* **2005**, *102*, 4294–4299.
- [16] G. Fusco, A. De Simone, T. Gopinath, V. Vostrikov, M. Vendruscolo, C. M. Dobson, G. Veglia, *Nat. Commun.* **2014**, *5*, 3827.
- [17] B. A. Shoemaker, J. J. Portman, P. G. Wolynes, *Proc. Natl. Acad. Sci. USA* **2000**, *97*, 8868–8873.
- [18] Y. Gu, D. W. Li, R. Bruschweiler, *J. Chem. Theory Comput.* **2014**, *10*, 2599–2607.
- [19] N. Salvi, A. Abyzov, M. Blackledge, *J. Phys. Chem. Lett.* **2016**, *7*, 2483–2489.

Manuscript received: July 17, 2018

Accepted manuscript online: September 5, 2018

Version of record online: October 18, 2018

Supporting Information

Local and Global Dynamics in Intrinsically Disordered Synuclein

Nasrollah Rezaei-Ghaleh, Giacomo Parigi, Andrea Soranno, Andrea Holla, Stefan Becker, Benjamin Schuler, Claudio Luchinat, and Markus Zweckstetter**

anie_201808172_sm_miscellaneous_information.pdf

Supplementary Methods

MD simulation

As described in ^[1], the MD simulation of α -synuclein was performed using the Amber12 force field with the TIP4P-D water model. The simulation started from an extended conformation of α -synuclein, solvated in an $\sim 100 \times 100 \times 100 \text{ \AA}^3$ box containing ~ 40000 water molecules and 0.1 M NaCl. The system was initially equilibrated at 300 K and 1 bar for 1 ns, then production run at 300 K and 1 bar was performed in the NPT ensemble with the Anton specialized hardware at 2.5 fs time step. Nonbonded interactions were truncated at 12 \AA and the Gaussian split Ewald method with a $64 \times 64 \times 64 \text{ \AA}$ mesh was used to account for the long-range part of the electrostatic interactions. The MD frames were saved at 10 ps intervals.

MD-based autocorrelation functions

Second-order orientational autocorrelation functions (ACF) between nuclei A and B (H-H for proton relaxometry or N-H for nitrogen relaxation) were calculated from the MD trajectory as ^[2]:

$$C(t) = \frac{1}{C_0} \left\langle \frac{D_{q,0}^{(2)*}(\Omega_0)}{r_0^3} \frac{D_{q,0}^{(2)*}(\Omega_t)}{r_t^3} \right\rangle \quad (\text{eq. S1})$$

where $D_{q,0}^{(2)}(\Omega)$ are the elements of the Wigner rotation matrix, $\langle \dots \rangle$ means ensemble averaging, the asterisk means complex conjugation, C_0 is the normalization constant (equal to $C(0)$), Ω s are different sets of Euler angles specifying the orientation of the AB vector with respect to the laboratory coordinate frame, r is the AB distance, and subscripted 0 and t denote the initial and final time moments at which r and Ω are calculated. To calculate spin relaxation rates, the relevant H-H or N-H ACFs were converted to spectral density functions through Fourier transformations. An exponential window function with a correlation time of 200 ns was applied to all ACFs to ensure that the artificially long components of motions in the MD trajectory do not affect the spectral density functions at very low frequencies. The ACFs were also fitted to multi-exponential decay functions,

$$C(t) = \sum_i S_i^2 \exp\left(-\frac{t}{\tau_i}\right) \quad (\text{eq. S2})$$

with $i = 1, 2, 3, 4, 5$ or 6 , where S_i^2 and τ_i represented the squared order parameters and correlation times corresponding to different motions, respectively, and $\sum S_i^2 = 1$. To evaluate the noise level in the ACFs, the MD trajectory was split into three (non-overlapping) sub-trajectories, each of 5 μs duration, and the ACFs were calculated separately for each sub-trajectory. The standard deviation between the three ACFs represented the noise level in the ACF of the whole trajectory.

Simulated proton relaxometry profiles

Fourier transformation of each pair of inter-proton ACFs provided individual spectral densities at different frequencies. The first 2- μs of the H-H ACFs were taken for Fourier transformation, as a result, spectral densities from 0 to 50 GHz at 0.5 MHz intervals were obtained. R_1 of all non-exchangeable CH_3 , CH_2 and CH^α protons were then calculated from the spectral densities, $J(\omega)$, through the equation ,

$$R_1(\omega) = \frac{3}{2} \left(\frac{\mu_0}{4\pi}\right)^2 \frac{\hbar^2 \gamma_H^4}{r^6} [0.2J(\omega) + 0.8J(2\omega)] \quad (\text{eq. S3})$$

in which $J(\omega) = \frac{\tau_R}{1 + \omega^2 \tau_R^2}$. The magnetization decay functions of all CH_3 , CH_2 and CH^α protons were then simulated as:

$$M(t) = M_0 \exp(-R_1 t) \quad (\text{eq. S4})$$

for t ranging from 0 to 1 s, and then the collective (experimentally detectable) magnetization decay function M_c was obtained from the average of magnetization decays of all protons. Finally, M_c was fitted with a double exponential decay function,

$$M_c(t) = M_0 (w_a \exp(-R_a t) + w_b \exp(-R_b t)) + M_{hf} \quad (\text{eq. S5a})$$

as it was done for the experimental data^[3] (the fit was in all cases very good, with a reduced χ^2 of about 10^{-5}), and the collective relaxation rate was defined as:

$$\langle R_1 \rangle = w_a R_a + w_b R_b \quad (\text{eq. S5b})$$

where w_a , R_a , R_b and M_{hf} were fitting parameters ($w_b=1-w_a$). The calculations were repeated for proton Larmor frequencies of 0.1, 0.5, 1, 2, 3, 5, 10, 15, 20 30 and 50, corresponding to the range of available experimental data^[3]. For R_1 calculation at $\omega=0.1$ MHz, $J(0.1\text{MHz})$ and $J(0.2\text{MHz})$ were approximated by $J(0)$. The resulting R_1 dispersion profile was then fitted to the following equation:

$$\langle R_1 \rangle = S_c^2 \langle E^2 \rangle \left(\frac{0.2\tau_R}{1+\omega_H^2\tau_R^2} + \frac{0.8\tau_R}{1+4\omega_H^2\tau_R^2} \right) + \alpha \quad (\text{eq. S6a})$$

which includes a single correlation time, or

$$\langle R_1 \rangle = \langle E^2 \rangle \left[S_{c(1)}^2 \left(\frac{0.2\tau_{R1}}{1+\omega_H^2\tau_{R1}^2} + \frac{0.8\tau_{R1}}{1+4\omega_H^2\tau_{R1}^2} \right) + S_{c(2)}^2 \left(\frac{0.2\tau_{R2}}{1+\omega_H^2\tau_{R2}^2} + \frac{0.8\tau_{R2}}{1+4\omega_H^2\tau_{R2}^2} \right) \right] + \alpha \quad (\text{eq. S6b})$$

with two correlation times. The $\langle E^2 \rangle$ was fixed to $2.4 \times 10^{10} \text{ s}^{-2}$, as previously calculated with CORMA^[3-4].

Simulated ¹⁵N relaxation rates

Second-order orientational ACFs for the 134 individual backbone N-H vectors of α -synuclein (all residues except M1 and prolines 108, 117, 120, 128 and 138) were calculated from the MD trajectory. Next, individual ACFs were converted to spectral density functions at different frequencies through Fourier transformation, as described above. Only the first 30-ns of the N-H ACFs, during which the ACFs generally decayed below 0.5% of the initial value, were taken for Fourier transformation. Then, ¹⁵N longitudinal (R_1) and transverse (R_2) auto-relaxation rates and transverse cross-correlated relaxation rates (CCR , η_{xy}) were calculated as:

$$R_1 = \left(\frac{d^2}{4} \right) [J(\omega_H - \omega_N) + 3J(\omega_N) + 6J(\omega_H + \omega_N)] + c^2 J(\omega_N) \quad (\text{eq. S7a})$$

$$R_2 = \left(\frac{d^2}{8} \right) [4J(0) + J(\omega_H - \omega_N) + 3J(\omega_N) + 6J(\omega_H) + 6J(\omega_H + \omega_N)] + \left(\frac{c^2}{6} \right) [4J(0) + 3J(\omega_N)] \quad (\text{eq. S7b})$$

$$\eta_{xy} = \frac{\sqrt{3}}{6} cdP_2(\cos\theta)[4J(0) + 3J(\omega_N)] \quad (\text{eq. S7c})$$

where $d = -\frac{\mu_0 \hbar \gamma_H \gamma_N}{4\pi r_{NH}^3}$ and $c = \frac{\gamma_N \Delta\sigma B_0}{\sqrt{3}}$. The effective NH bond length of 1.04 Å was used to account for zero-point vibrations^[5] and the ¹⁵N CSA tensor magnitudes ($\Delta\sigma$) were set to -170 ppm. The angle θ between NH bond vectors and the main axis of the ¹⁵N CSA tensors was set to 22.5°^[6]. To optimize the scaling factors for the correlation times and/or the order parameters corresponding to different motions present in the MD-derived N-H ACFs, the spectral density functions at angular frequency ω were first calculated using the best-fit parameters obtained with three-exponential decay function as:

$$J(\omega) = \frac{2}{5} \left(S_{slow}^2 \frac{\tau_{slow}}{1+(\omega\tau_{slow})^2} + S_{int}^2 \frac{\tau_{int}}{1+(\omega\tau_{int})^2} + S_{fast}^2 \frac{\tau_{fast}}{1+(\omega\tau_{fast})^2} \right) \quad (\text{eq. S8})$$

and subsequently the relaxation rates R_1 and R_2 were predicted through equations 7a-b. The optimal temporal and order parameter scaling factors were then obtained through minimization of the relative root mean square of deviation (rmsd) between the experimental and predicted relaxation rates, as:

$$rmsd = \sqrt{\left[\left(\frac{R_{1,pred}-R_{1,exp}}{R_{1,exp}}\right)^2 + \left(\frac{R_{2,pred}-R_{2,exp}}{R_{2,exp}}\right)^2\right]/2} \text{ (eq. S9)}$$

Experimental ^{15}N relaxation rates

^{15}N R_1 and R_2 rates, ^1H , ^{15}N heteronuclear NOE and transverse cross-correlated relaxation rates (CCR , η_{xy}) of α -synuclein were measured at a proton Larmor frequency of 600 MHz (and in case of R_2 , also at 800 MHz) using AVANCE-III Bruker (Karlsruhe, Germany) spectrometers. The uniformly ^{15}N -labeled NMR sample contained ~ 1 mM α -synuclein at pH 5.0 dissolved in 10% D_2O /90% H_2O . The temperature was set to 25 °C. The pH and temperature were identical to those used for experimental proton relaxometry experiments [3]. ^{15}N R_1 rates were measured using conventional pulse sequence schemes with ten relaxation delays between 10 and 1000 ms [7]. ^{15}N R_2 rates were obtained using a CPMG-based scheme with a τ_{cp} of 1 ms and relaxation delays of 12, 32, 52, 72, 92, 112, 132, 152 and 172 ms [7]. R_1 and R_2 relaxation rates were determined by fitting the corresponding peak intensities to a single exponential decaying function. Errors in relaxation rates were estimated from 500 Monte Carlo (MC) simulation runs for which the fit residuals were taken as the random noise. Steady-state hetNOEs were obtained by comparison of peak intensities between saturated and reference spectra, where the duration of saturation block and the total recycle delay in the hetNOE were 5 and 8 s, respectively. The R_1 , R_2 and hetNOE measurements were performed in FID-interleaved manner. The CCR rates were measured using relaxation delays of 100, 150 and 200 ms [8]. The exchange-free R_2 rates, R_2^0 , were derived from CCR as described in [9]. Reduced spectral density mapping analysis of ^{15}N relaxation rates [10] was made using an in-house MATLAB script.

Single-molecule fluorescence spectroscopy

Labeling of α -synuclein with Alexa Fluor 488 and 594 for single-molecule FRET measurements. A double-cysteine variant of α -synuclein (S42C and T92C) was reduced with 1,4-Dithiothreitol (DTT) and subsequently purified by RP-HPLC using a Reprosil Gold C18 column with a water-acetonitrile (ACN) gradient (Solvent A: 0.1% TFA, Solvent B: ACN; gradient: 5-50% B in 30 min). The protein was labeled with the donor dye Alexa Fluor 488 maleimide in 6 M guanidinium chloride (GdmCl), 100 mM sodium phosphate, pH 7.3, overnight at 4°C at a molar ratio of dye to protein of 0.7:1. The reaction was stopped by adding DTT. A gradient of 37-42% B over 30 min was chosen to separate unlabeled, singly and doubly donor-labeled protein on the Reprosil Gold C18 column. Singly labeled material was further labeled with the acceptor dye Alexa Fluor 594 maleimide at a molar ratio of dye to protein of 5:1 for 4 h at room temperature. Unreacted dye was quenched with DTT. Purification of donor-acceptor labeled protein was achieved by RP-HPLC as described above. The mass of donor/acceptor-labelled α -synuclein was confirmed by ESI-MS.

Single-molecule fluorescence spectroscopy.

Single-molecule fluorescence measurements were conducted on a MicroTime 200 confocal microscope (PicoQuant, Germany). Labeled molecules were excited with a diode laser (LDH-D-C-485, PicoQuant, Germany) in continuous-wave mode. Emitted fluorescence was collected by the objective (UplanApo 60x/1.20W, Olympus) and filtered (HQ500LP, Chroma Technology) before passing the confocal pinhole (100 μm diameter). The emitted photons were then sorted into four channels, first by a polarizing beam splitter and then by a dichroic mirror (585DCXR, Chroma) for each polarization. Donor and acceptor emission was filtered (ET525/50m or HQ650/100m, respectively, Chroma Technology) and then focused

on a τ -SPAD avalanche photodiode (PicoQuant). The arrival time of every detected photon was recorded with a HydraHarp 400 counting module (PicoQuant).

FRET efficiency and intramolecular distances. Fluorescence bursts from individual molecules were identified by combining successive photons separated by inter-photon times of less than 150 μ s and retaining the burst only if the total number of photons detected after donor excitation was greater than 40. Transfer efficiencies for each burst were calculated according to $E = n_A / (n_A + n_D)$, where n_D and n_A are the numbers of donor and acceptor photons, respectively, corrected for background, acceptor direct excitation, channel crosstalk, differences in detector efficiencies, and quantum yields of the dyes^[11]. The histogram of transfer efficiencies was fitted with two empirical peak functions, using a normal distribution for both the donor-only and the FRET populations. Mean values of transfer efficiency $\langle E \rangle$ corresponding to the unfolded population were related to the distance information by solving numerically

$$\langle E \rangle = \int E(r)P(r)dr \quad (\text{eq. S10})$$

for which we assumed for $P(r)$ the distance distribution of a random walk (Gaussian) chain,

$$P(r) = 4\pi r^2 \left(\frac{3}{2\pi R^2} \right)^{3/2} \exp\left(-\frac{3r^2}{2R^2}\right) \quad (\text{eq. S11a})$$

where R is the root-mean-squared distance between the dyes. The mean distance inferred in this way was robust to the choice of polymer models to within 6% when distance distributions for a worm-like chain^[12]

$$P_{WLC}(r) = Z \frac{4\pi(r/l_c)^2}{l_c[1-(r/l_c)^2]^{9/2}} \exp\left(\frac{-3l_c}{4l_p[1-(r/l_c)^2]}\right) \quad (\text{eq. S11b})$$

or an excluded volume chain^[13]

$$P_{SAW}(r) = 4\pi r^2 \frac{0.278}{R^3} \left(\frac{r}{R}\right)^{0.28} \exp(-1.206\left(\frac{r}{R}\right)^{2.43}) \quad (\text{eq. S11c})$$

were used (l_c is the contour length of the chain and Z is a normalization factor). Note that the distribution of transfer efficiency observed for the peak in the histogram (Figure S3) is dominated by shot noise, because the dynamics of inter-dye distance fluctuations is faster than the average interphoton time, and can thus not be used to infer a distance distribution directly^[14]. Finally, to account for the length of dye linkers and compare the experimental data with simulations, R was rescaled to the distance between residues m and n according to

$$R_{m,n} = R \frac{|m-n|^{0.5}}{|m-n+2l|^{0.5}} \quad (\text{eq. S12})$$

with $l = 4.5$ corresponding to the effective number of amino acid residues equivalent to one of the dyes with its linker^[15].

Reconfiguration times from FRET-FCS. Autocorrelation curves of acceptor and donor channels and cross-correlation curves between acceptor and donor channels were computed from the measurements and analyzed as described previously^[16]. The data were fitted over different time windows, from 1 μ s to 5 μ s (to assess the robustness of the fit), according to

$$g_{ij}(\tau) = 1 + \frac{1}{N} \left(1 - c_{AB} e^{-\frac{\tau-t_0}{\tau_{AB}}}\right) \left(1 + c_{CD} e^{-\frac{\tau-t_0}{\tau_{CD}}}\right) \left(1 + c_T e^{-\frac{\tau-t_0}{\tau_T}}\right) \quad (\text{eq. S13a})$$

and

$$g_{ij}(\tau) = 1 + \left(\frac{f}{N} \left(1 + c_{CD} e^{-\frac{t-t_0}{\tau_{CD}}} \right) + \frac{1-f}{N} \left(1 + c_{CD2} e^{-\frac{t-t_0}{\tau_{CD2}}} \right) \right) \left(1 - c_{AB} e^{-\frac{t-t_0}{\tau_{AB}}} \right) \left(1 + c_T e^{-\frac{t-t_0}{\tau_T}} \right),$$

$$i, j = A, D \quad (\text{eq. S13b})$$

where N is the mean number of molecules in the confocal volume, c_{AB} , c_{CD} , c_{CD2} and c_T are the amplitudes related to photon antibunching (AB), chain dynamics (CD) and triplet blinking of the dyes (T), τ_{AB} , τ_{CD} , τ_{CD2} and τ_T are the corresponding relaxation times, f is the fraction of protein associated with the relaxation time τ_{CD} (for simplicity, brightness of the two fractions was considered to be identical). The relaxation times were extracted by fitting the three curves globally to eq. S13, assuming the same values of τ_{CD} but distinct triplet times for the three correlations. Assuming that chain dynamics can be described as a diffusive process in the potential of mean force derived from the sampled distance distribution $P(r)$ ^[17], we convert τ_{CD} and τ_{CD2} to the reconfiguration time of the chain, τ_r ^[16a]. Note that τ_{CD} and τ_r differ by only 6% in the present case because the root-mean-square distance is close to the Förster radius ^[16a].

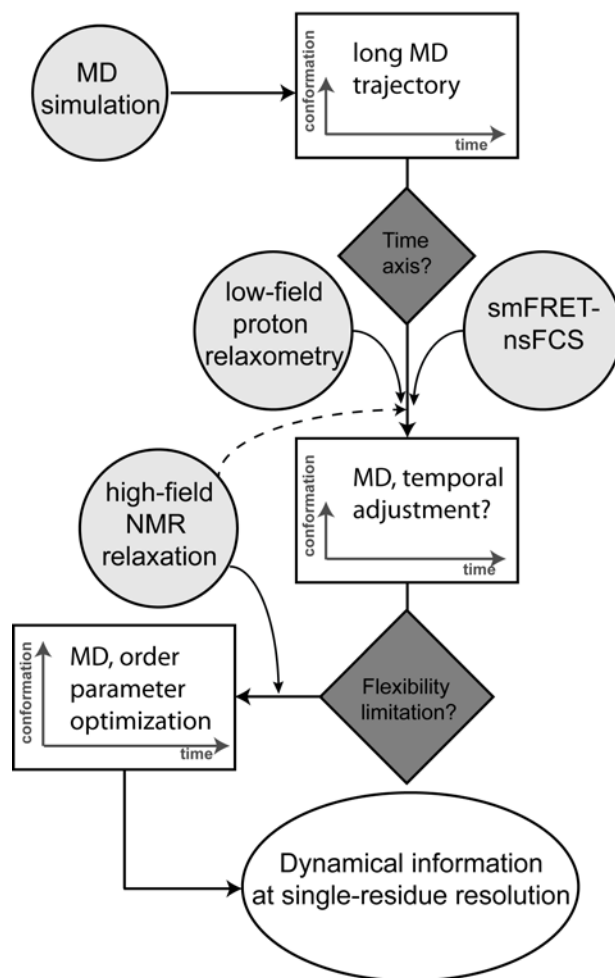


Figure S1. Flowchart representation of the approach of this study for investigating IDP dynamics through combination of MD simulation, low-field proton relaxometry, single-molecule FRET-nsFCS and high-field ^{15}N spin relaxation. It starts with a long MD simulation of the IDP of interest with the optimized force-field and water models. The duration of the MD simulation should be at least several microseconds to converge the longest dynamics expected for the IDP. Then, a careful analysis of experimental and simulated proton relaxometry profiles will provide correlation times of reorientational motions, and thus a global time axis scaling factor for the MD trajectory. The temporal adjustment of the MD trajectory can be further supported by single-molecule FRET-nsFCS data, which report chain reconfiguration dynamics in tens to hundreds of nanoseconds. Following temporal adjustment of the MD trajectory, high-field ^{15}N relaxation rates will be employed to detect local flexibility limitations in MD and optimizing order parameters at single-residue level. The approach of this study may be called “IASMIN”, for the Integrative Approach for Scaling of Molecular dynamic simulation for Intrinsically disordered proteins.

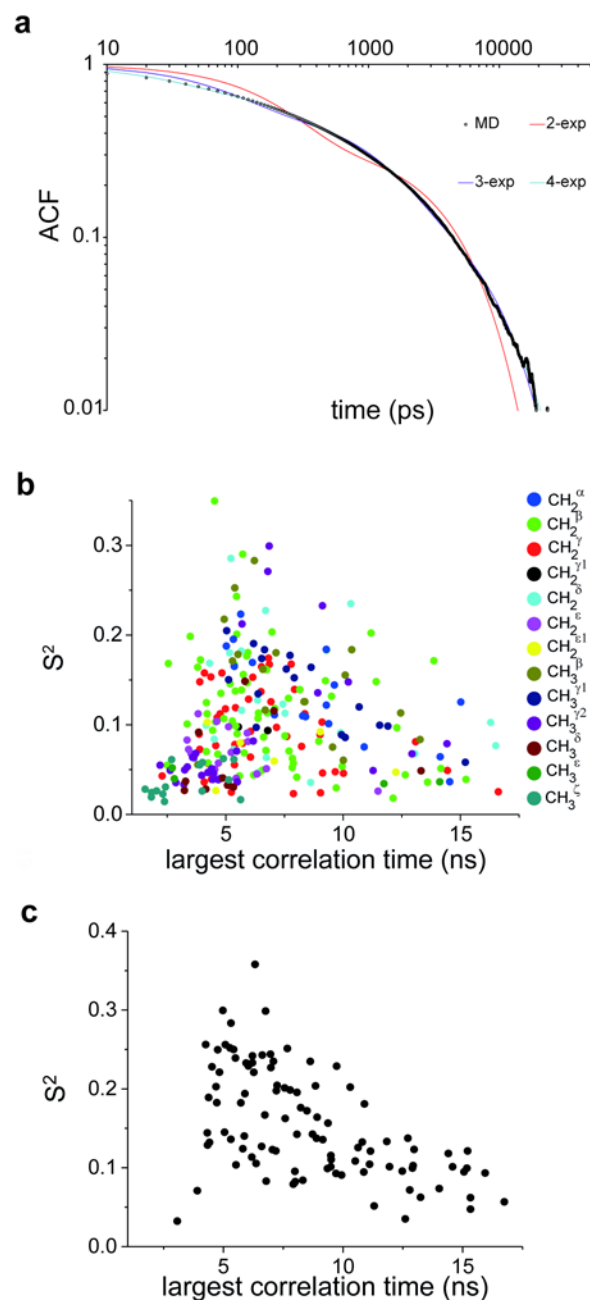


Figure S2. MD-based proton-proton angular autocorrelation functions (ACF). (a) The ACF of a representative H-H pair (gray circles), and its best-fit curves to two-, three- or four-exponential decay functions (solid lines). The decaying behavior of the ACF during the first 1000 ps is satisfactorily captured only when four exponential terms are included. (b,c) Longest correlation times and corresponding squared order parameters obtained from the fit of the MD-based ACFs of methylene and methyl protons (b) and CH^α protons (c). A large spread of correlation times and order parameters is observed over protein protons.

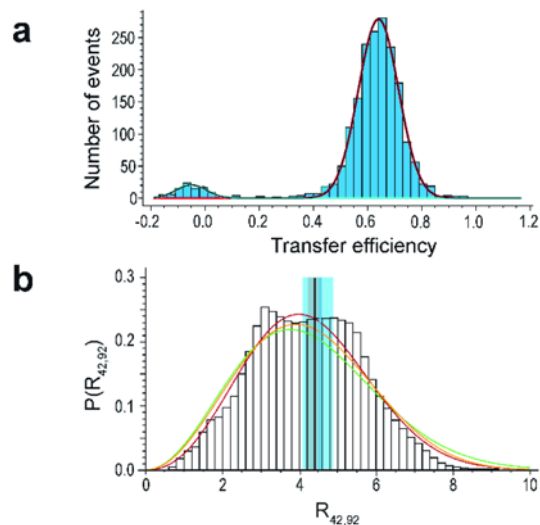


Figure S3. Single-molecule FRET of double-labeled S42C/T92C α -synuclein. (a) FRET efficiency histogram. The mean value of the transfer efficiency is 0.64, corresponding to an inter-dye distance of 4.7 ± 0.2 , 5.0 ± 0.2 , and 4.6 ± 0.2 nm assuming a Gaussian, wormlike or a self-avoiding random walk, respectively. The small peak at zero FRET efficiency is due to molecules without active acceptor fluorophore. (b) Distance distributions of simple polymer models approximate the shape of the probability distribution for the C^α - C^α distance between residues 42 and 92 obtained from the MD simulation. The resulting root-mean-square-distances are: 4.6 nm (fit to Gaussian chain, green), 4.5 nm (fit to wormlike chain, orange), and 4.4 nm (fit to self-avoiding random walk, red). The root-mean-square distance calculated from the simulation data is 4.4 ± 0.2 (black vertical line and gray shaded area). The corresponding experimental values are reported for comparison (cyan vertical line and shaded area).

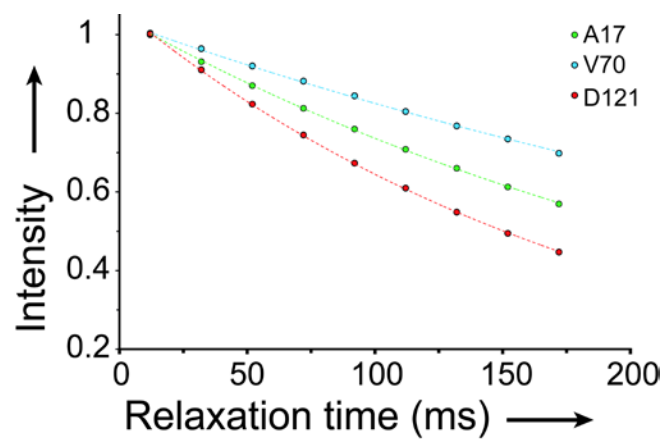


Figure S4. Experimental determination of ^{15}N relaxation rates. As typical examples, the intensity decay of three residues from the N-terminal, NAC and C-terminal regions (A17, V70 and D121, highlighted in Fig. 1d) in R_2 experiments are shown.

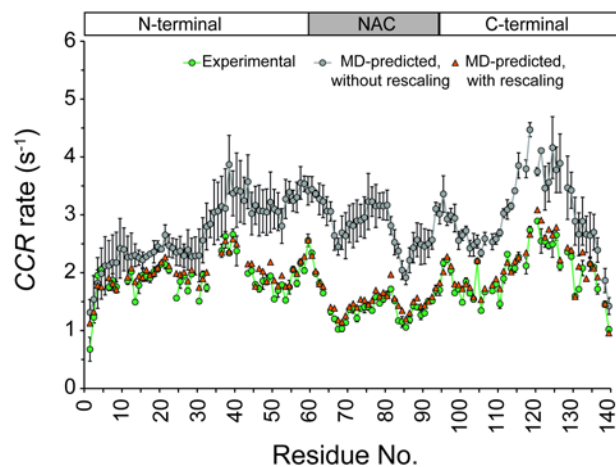


Figure S5. Residue-specific cross-correlated relaxation (CCR) rate between ^1H , ^{15}N dipole-dipole and ^{15}N chemical shift anisotropy relaxation of α -synuclein, measured at 600 MHz proton Larmor frequency and 25 °C (green circles/lines). The rates calculated from the 16- μs MD trajectory are shown as gray circles, with the error bars representing the standard deviation between the rates calculated from three MD sub-trajectories, each of 5 μs duration. The predicted rates after rescaling of the MD are shown as orange triangles.

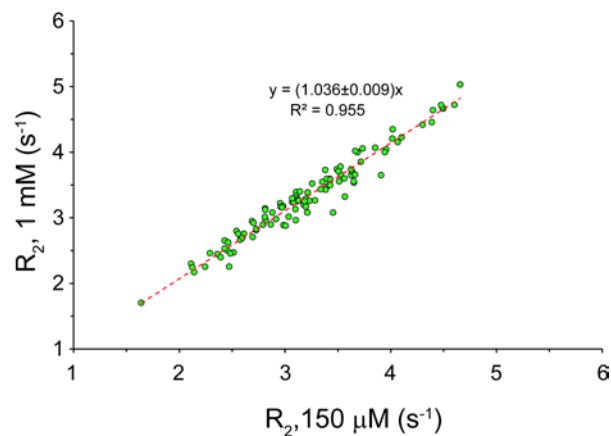


Figure S6. Comparison of ^{15}N R_2 relaxation rates of α -synuclein, measured at two different protein concentrations (1 mM and 150 μM). The ^{15}N relaxation rate measurements were performed at 800 MHz proton Larmor frequency and 25 $^\circ\text{C}$. Since highly similar relaxation rates are obtained at these two protein concentrations, the possibility that α -synuclein aggregation makes a significant contribution to ^{15}N relaxation rates is excluded. The linear slope of 1.027-1.045 (95% CI) can be explained by the higher viscosity of the 1 mM α -synuclein sample, compared to the more dilute 150 μM sample. If we approximate that the R_2 is determined exclusively by $J(0)$ and ignore the small contributions from higher frequency terms, then an intrinsic viscosity of 2.21-3.69 cm^3/g (95% CI) would be required to explain the observed ratio of R_2 at two concentrations. The estimated value of intrinsic viscosity for α -synuclein is comparable to the intrinsic viscosities obtained for a broad range of proteins^[18].

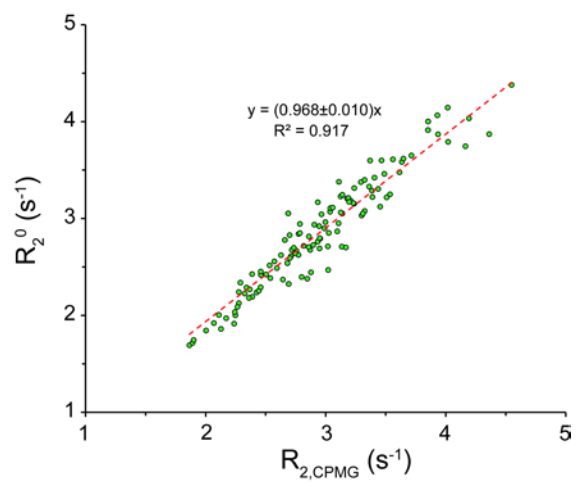


Figure S7. The exchange-free R_2 rates (R_2^0) calculated from *CCR* rates are in close agreement with the R_2 rates used for spectral density analysis, indicating that the deviation from single-Lorentzian behavior (shown in Figure S8) is unlikely to be caused by exchange contributions to relaxation rates. The reported slope represents 95% CI.

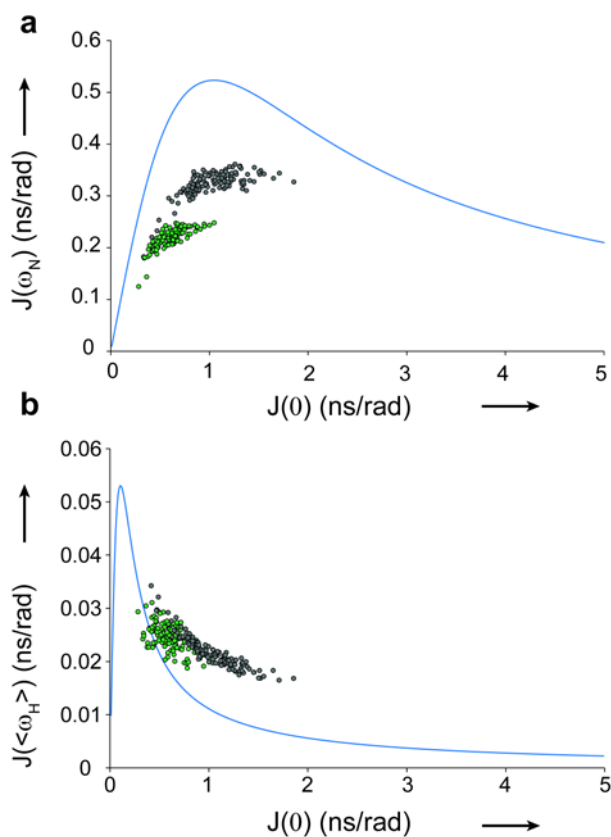


Figure S8. Spectral density analysis of experimental ^{15}N relaxation rates, shown here as $J(0)$ dependence of $J(\omega_N)$ (a, green circles) or $J(\langle\omega_H\rangle)$ (b, green circles), indicates that fast dynamics of α -synuclein backbone cannot be described by single-Lorentzian motions, i.e. motions with a single correlation time (blue curve). The MD-derived spectral density functions are shown by gray circles. The comparison between experimental (green circles) and simulated (gray circles) spectral density functions point to a general overestimation of $J(0)$ and $J(\omega_N)$ by MD.

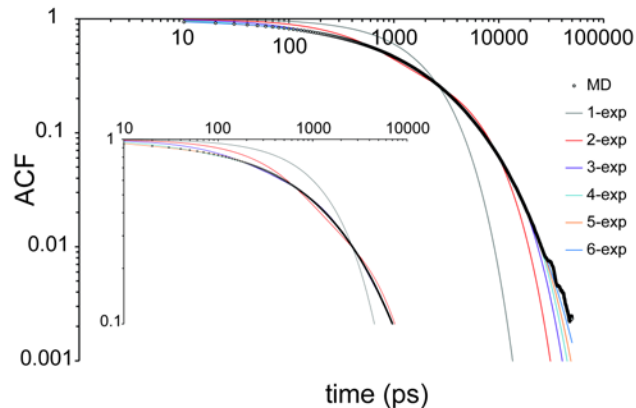


Figure S9. The global angular autocorrelation function (ACF) of N-H groups calculated from the MD trajectory (gray circles), fitted to a multi-exponential function with 1 to 6 exponential terms (solid lines). Successive addition of the exponential terms led to significant improvement in the quality of fit (P-value <0.0001), however inclusion of only three exponential terms was sufficient to lower the deviation between the simulation and fitted ACFs below the noise level in ACF. As a result, in accord with recent studies of IDP dynamics at multiple fields^[19] and temperatures^[20], we decided to fit residue-specific ACFs with three-exponential decay functions. As shown in the Inset, the fit in the first 100 ps of the ACF is sub-optimal when less than four exponential terms are included in the model. The MD-derived ACF exhibits some irregularities following ~ 30 ns, therefore only the initial 30 ns of the ACF were used for fitting.

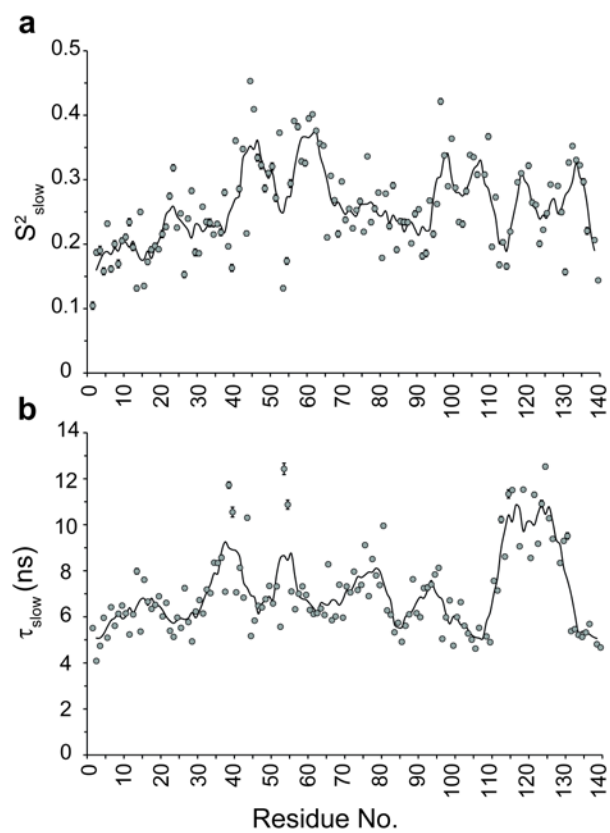


Figure S10. MD-based squared order parameters, S^2_{slow} (a), and correlation times, τ_{slow} (b), obtained from the fitting of angular autocorrelation functions of individual N-H vectors to a three-exponential decay function. Error bars, representing 95% CI, are mostly smaller than the symbol size. The solid lines show averaged values over a five-residue window.

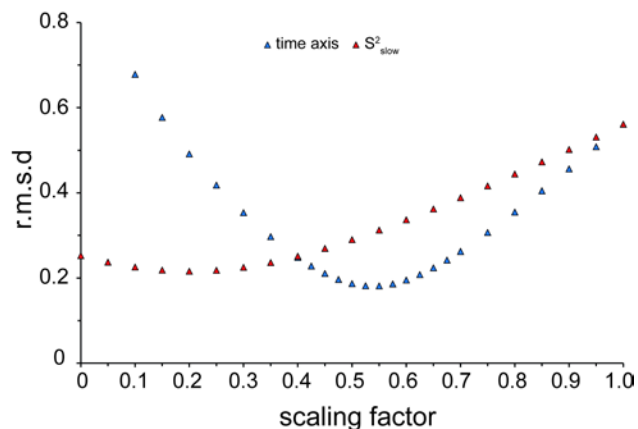


Figure S11. Dependence of the quality of fit between experimental and MD-predicted ^{15}N relaxation rates (R_1 , R_2 and CCR at 600 MHz and R_2 at 800 MHz) on the global time axis (blue triangle) or S^2_{slow} (red triangle) rescaling of the MD trajectory. The best agreement between experimental and MD-predicted rates could be achieved after temporal adjustment by a factor of 0.55 or S^2_{slow} scaling of 0.20. For S^2_{slow} rescaling, the MD-based S^2_{slow} was multiplied by the specified scaling factor, then the order parameters of fast (S^2_{fast}) and intermediate (S^2_{int}) motions were accordingly re-scaled to keep $\sum S_i^2 = 1$ ($i=1,2,3$ for fast, intermediate and slow motions). The r.m.s.d was calculated as $rmsd = \sqrt{\left[\left(\frac{R_{1,pred}-R_{1,exp}}{R_{1,exp}}\right)^2 + \left(\frac{R_{2,pred}-R_{2,exp}}{R_{2,exp}}\right)^2 + \left(\frac{CCR_{pred}-CCR_{exp}}{CCR_{exp}}\right)^2 + \left(\frac{R_{2,800,pred}-R_{2,800,exp}}{R_{2,800,exp}}\right)^2\right] / 4}$.

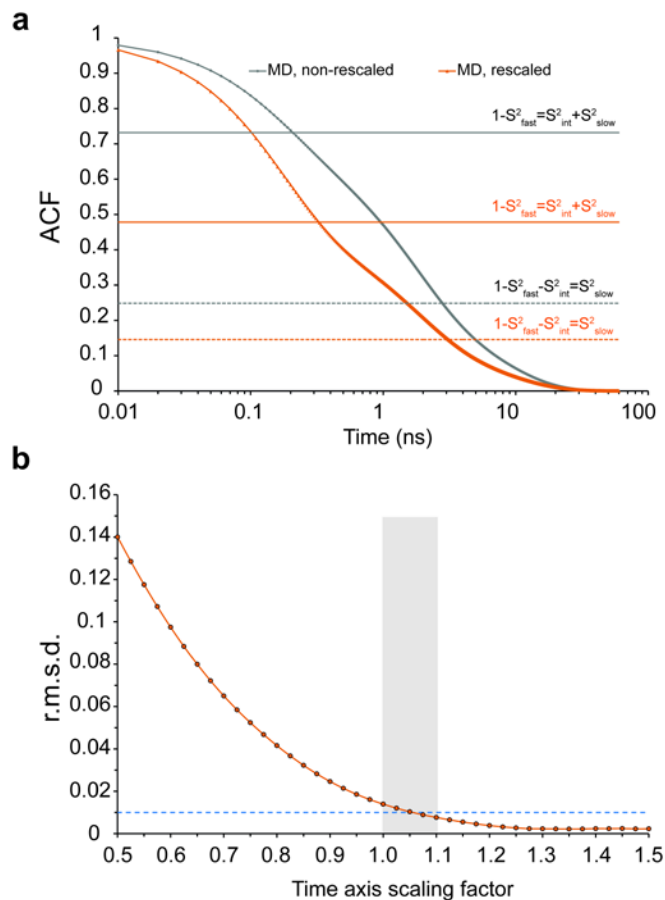


Figure S12. Optimization of MD-derived order parameters on the basis of ^{15}N relaxation rates, R_1 and R_2 at 600 MHz. (a) The best agreement with the experimental ^{15}N relaxation rates could be achieved through global time axis rescaling of the MD trajectory and optimization of the MD-derived order parameters. The average N-H autocorrelation function (ACF) is shown before (gray curve) and after (orange curve) such rescaling. The gray lines demonstrate how much of the N-H orientational memory remains in the MD-derived average ACF after fast (solid line) and intermediate (dotted line) motions are completed. The orange lines show the corresponding levels after rescaling of the average ACF. (b) Dependence of the quality of fit on the global time axis rescaling of the MD trajectory, while the order parameters are accordingly optimized. An excellent agreement could be achieved with time axis scaling factors at or above 1.05. In line with the proton relaxometry and nsFCS data, a time scaling factor of 1.05 ± 0.05 was used during order parameter optimization (shaded area).

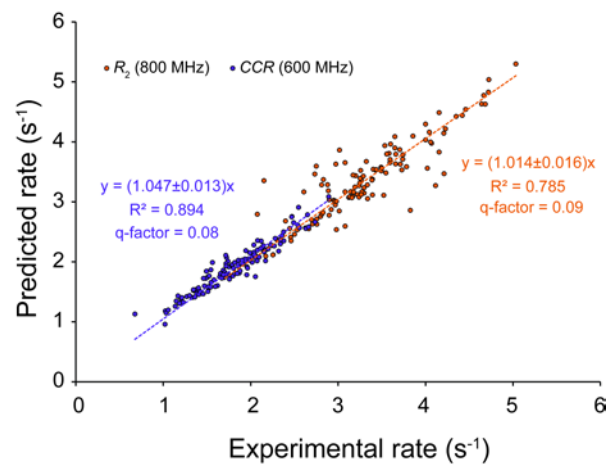


Figure S13. Cross-validation of optimized MD-based order parameters by $R_{2,800\text{MHz}}$ (orange circles) and $CCR_{600\text{MHz}}$ (purple circles) rates. The predicted rates fit reasonably well to the experimental values.

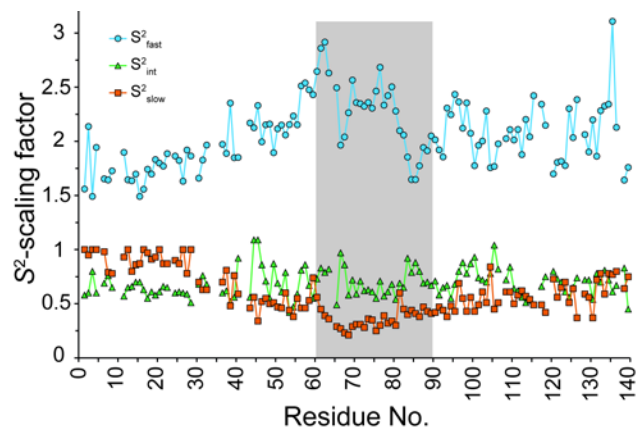


Figure S14. Degree of order parameter rescaling along α -synuclein sequence, reflecting the extent of local flexibility limitation in the MD trajectory. As indicated by the sequence dependence of S^2_{slow} scaling factor, the NAC region (shaded area) exhibit severe conformational sampling limitation, while the N-terminal residues 1-30 are least affected.

Table S1. Comparison of average intramolecular distances from single-molecule FRET and MD simulation

	$R_{42,92}$ (nm)			
	single-molecule FRET	MD simulation ^a	MD simulation best fit ^b	MD simulation from computed E ^c
Rms distance	-	4.4±0.2		
Gaussian chain	4.7±0.2	-	4.6	4.71
WLC ^d	4.6±0.2	-	4.5	5.06
SAW ^e	4.4±0.2	-	4.4	4.46

^a Mean and standard deviation estimated by subdividing the simulation in 5 μ s segments. ^b Root-mean-squared distance estimated from the best fit of the different polymer models to the simulated distance distribution. ^c Root-mean-squared distance estimated with the different polymer models from the mean transfer efficiency computed from the simulated data. ^d Worm-like chain. ^e Self-avoiding random walk chain

Table S2. Fitting of the MD-derived global N-H angular autocorrelation function (ACF) of α -synuclein to multi-exponential decay functions with up to six exponential terms

	τ_1^a (S^2_1)	τ_2 (S^2_2)	τ_3 (S^2_3)	τ_4 (S^2_4)	τ_5 (S^2_5)	τ_6 (S^2_6)	SSE ^b
1-exp	1962±28 (1)	-	-	-	-	-	7.5160
2-exp	544±9 (0.57)	5122±51 (0.43)	-	-	-	-	0.3864
3-exp	152±3 (0.27)	1545±16 (0.48)	7321±51 (0.25)	-	-	-	0.0301
4-exp	41±1 (0.13)	512±6 (0.29)	2332±20 (0.41)	8666±45 (0.18)	-	-	0.0036
5-exp	13±0 (0.08)	211±3 (0.17)	1001±11 (0.32)	3321±32 (0.32)	10130±63 (0.12)	-	0.0005
6-exp	7±0 (0.05)	100±1 (0.09)	466±5 (0.21)	1619±15 (0.34)	4980±62 (0.25)	13635±238 (0.06)	<0.0001

^a Correlation times (τ_i) in picosecond. 95% CIs are shown. The fitting error for squared order parameters (S^2_i , $i=1$ to 6) were generally <0.01. ^b Sum of Squared Errors. After successive inclusion of exponential terms from 1 to 6 terms, the quality of fit was significantly improved (P-value < 0.0001). Inclusion of only three exponential terms was sufficient to lower the deviation between the simulation and fitted ACFs below the noise level in ACF of 0.089. To evaluate the noise level in the ACF, the global ACFs were calculated for three non-overlapping MD sub-trajectories, each of 5 μ s duration, and the average SSE between them and the average ACF was calculated.

Table S3. Overall comparison of experimental ^{15}N R_1 and R_2 , ^1H , ^{15}N heteronuclear NOE and CCR rates of α -synuclein with the rates predicted from the 16- μs MD trajectory of α -synuclein, calculated using Amber12 force field with sampling interval of 10 ps

		Experimental	MD-predicted	MD-predicted (time-rescaled) ^b	MD-predicted (S^2 -rescaled) ^c
R_1	at 600 MHz (s^{-1}) ^a	1.39±0.10	1.62±0.07 (0.25)	1.59±0.14 (0.22)	1.75±0.17 (0.39)
R_2	at 600 MHz (s^{-1})	2.94±0.56	4.16±0.77 (1.38)	2.71±0.51 (0.51)	2.73±0.52 (0.52)
CCR	at 600 MHz (s^{-1})	1.81±0.42	2.83±0.56 (1.13)	1.78±0.37 (0.36)	1.78±0.37 (0.36)
hetNOE	at 600 MHz	-0.15±0.17	0.11±0.15 (0.29)	-0.10±0.22 (0.20)	-0.02±0.17 (0.21)
R_2	at 800 MHz (s^{-1})	3.30±0.64	5.00±0.95 (1.89)	3.05±0.60 (0.58)	3.07±0.58 (0.59)

^a Errors are standard deviation of the experimental and MD-predicted rates over α -synuclein residues. In parentheses, the r.m.s.d. between experimental and MD-predicted rates are shown. ^b The time axis of the MD trajectory was rescaled by multiplying to 0.55. ^c The MD-based order parameter of the slow motion (S^2_{slow}) was multiplied by 0.20, then the order parameters of the fast (S^2_{fast}) and intermediate (S^2_{inter}) motions were accordingly re-scaled to keep $\sum S_i^2 = 1$.

References

- [1] S. Piana, A. G. Donchev, P. Robustelli, D. E. Shaw, *J Phys Chem B* **2015**, *119*, 5113-5123.
- [2] Y. E. Ryabov, D. Fushman, *J Am Chem Soc* **2007**, *129*, 3315-3327.
- [3] G. Parigi, N. Rezaei-Ghaleh, A. Giachetti, S. Becker, C. Fernandez, M. Blackledge, C. Griesinger, M. Zweckstetter, C. Luchinat, *J Am Chem Soc* **2014**, *136*, 16201-16209.
- [4] B. A. Borgias, P. D. Thomas, T. L. James, *Abstr Pap Am Chem S* **1989**.
- [5] D. A. Case, *J Biomol NMR* **1999**, *15*, 95-102.
- [6] P. Kaderavek, V. Zapletal, A. Rabatinova, L. Krasny, V. Sklenar, L. Zidek, *J Biomol NMR* **2014**, *58*, 193-207.
- [7] A. G. Palmer, 3rd, *Annu Rev Biophys Biomol Struct* **2001**, *30*, 129-155.
- [8] N. Tjandra, A. Szabo, A. Bax, *J Am Chem Soc* **1996**, *118*, 6986-6991.
- [9] N. Rezaei-Ghaleh, K. Giller, S. Becker, M. Zweckstetter, *Biophys J* **2011**, *101*, 1202-1211.
- [10] N. A. Farrow, O. Zhang, J. D. Forman-Kay, L. E. Kay, *Biochemistry* **1995**, *34*, 868-878.
- [11] B. Schuler, S. Muller-Spath, A. Soranno, D. Nettels, *Methods Mol Biol* **2012**, *896*, 21-45.
- [12] E. P. O'Brien, G. Morrison, B. R. Brooks, D. Thirumalai, *J Chem Phys* **2009**, *130*, 124903.
- [13] A. V. Dobrynin, M. Rubinstein, *J Physique II* **1995**, *5*, 677-695.
- [14] B. Schuler, H. Hofmann, A. Soranno, D. Nettels, *Annu Rev Biophys* **2016**, *45*, 207-231.
- [15] aA. Hoffmann, A. Kane, D. Nettels, D. E. Hertzog, P. Baumgartel, J. Lengefeld, G. Reichardt, D. A. Horsley, R. Seckler, O. Bakajin, B. Schuler, *Proc Natl Acad Sci U S A* **2007**, *104*, 105-110; bM. Aznauryan, L. Delgado, A. Soranno, D. Nettels, J. R. Huang, A. M. Labhardt, S. Grzesiek, B. Schuler, *Proc Natl Acad Sci U S A* **2016**, *113*, E5389-5398.
- [16] aI. V. Gopich, D. Nettels, B. Schuler, A. Szabo, *J Chem Phys* **2009**, *131*, 095102; bA. Soranno, B. Buchli, D. Nettels, R. R. Cheng, S. Muller-Spath, S. H. Pfeil, A. Hoffmann, E. A. Lipman, D. E. Makarov, B. Schuler, *Proc Natl Acad Sci U S A* **2012**, *109*, 17800-17806.
- [17] D. Nettels, I. V. Gopich, A. Hoffmann, B. Schuler, *Proc Natl Acad Sci U S A* **2007**, *104*, 2655-2660.
- [18] D. K. Hahn, S. R. Aragon, *J Chem Theory Comput* **2006**, *2*, 1416-1428.
- [19] M. L. Gill, R. A. Byrd, A. G. Palmer, III, *Phys Chem Chem Phys* **2016**, *18*, 5839-5849.
- [20] A. Abyzov, N. Salvi, R. Schneider, D. Maurin, R. W. Ruigrok, M. R. Jensen, M. Blackledge, *J Am Chem Soc* **2016**, *138*, 6240-6251.